Miniature Compliance Controllable Sensor for Tissue Stiffness Sensing and Palpation

Duncan G. Raitt[1], Shervanthi Homer-Vanniasinkam[1], Prokar Dasgupta[2], Sara-Adela Abad[1,3], *Member, IEEE* and Helge A. Wurdemann[1], *Member, IEEE*

***Abstract*—Tissue stiffness can provide key details about the health and type of tissues. This paper presents the creation of a miniaturised soft tissue stiffness sensor with dimensions that make it suitable for palpation in minimally invasive surgery. We introduce the stiffness sensor design and experimentally test its force sensing, elasticity measurement, and dynamic palpation performance. The sensor can measure normal forces with an adjustable range. Angled forces were measured with their magnitude and angles, θ_Y and θ_X, root-mean-square errors (RMSE) of 8.37%, 6.68%, and 13.92% of their respective ranges. Furthermore, samples with an elasticity between 4.20 kPa and 177.62 kPa, which were not in the training set, were measured with an RMSE of 7.79% of the tested range. During palpation, the boundary between the 13.4 kPa elastomer and the 2 mm embedded 29.3 kPa elastomer was located with a signal-noise ratio (SNR) of 77.04:1 and a mean offset of 0.706 mm. This investigation provides new insights into sensing devices capable of fitting trocars while measuring tissue elasticity and force during minimally invasive procedures.**

***Index Terms*—Sensor, Stiffness, Force, Palpation, Surgical**

I. Introduction

In biomedical applications, the sense of touch allows clinicians to assess tissue health and locate stiffer and softer regions during palpation. Haptic sensors [1]–[4] and probes [5], [6] have been produced to measure forces, quantify tissue stiffness, or locate areas of different stiffness during dynamic palpation. From these, several sensors have demonstrated multiple of these functions.

Farragasso et al. developed a sensor to measure stiffness and carry out dynamic palpation [1]. This was achieved through optically tracking sprung indenters of different stiffness interacting with the tissue. This device could measure the spring stiffness of 0.29 N/mm and 0.62 N/mm samples at angles up to 20° with maximum errors of 6.4% of sample stiffness. In robotic and handheld palpation this device could also create a map of tissue stiffness. It interacted using stiff tips increasing the likelihood of tissue damage and had a diameter of over 25 mm, preventing it from being inserted through any commonly available trocars.

Gelsight sensors have been shown to measure sample hardness, detect embedded nodules and sense forces. Yuan et al. demonstrated that using a neural network, this sensor could measure the hardness of objects it was being pushed onto [2]. Samples ranging in hardness from 00-8 Shore hardness to 00-87 Shore hardness were tested. These were made from elastomers which range in elasticity from around 55 kPa to around 827 kPa. Samples of trained shapes but untrained hardness were measured with a root-mean-square error (RMSE) of 00-5.18, 5.95% of the tested range. When pressed against embedded nodules by Jia et al. a gelsight sensor was able to detect the presence of 2 mm nodules at depths of up to 5 mm [3]. Yuan et al. also showed that a gelsight sensor could measure the magnitude of normal forces applied by flat objects pushed against it with an RMSE of 1.857 N [4]. Li et al. and Lu et al. expanded on this showing that these sensors could measure 3-axis forces, along with torsional angles [7], [8]. These papers pushed the normal force sensing accuracy to an RMSE of 0.033 N. Kara et al. demonstrated a similar sensor's ability to classify colorectal cancer polyps both using phantoms and ex-vivo samples [9]. However, these sensors all had outer diameters over 35 mm which is too large to fit through trocars for use in MIS.

Tactip sensors have been shown to measure forces and identify embedded nodules. Giannaccini et al. [10] tested the Tactip sensor's force sensing abilities. A robot arm pressed the Tactip sensor onto a flat load cell which measured the corresponding forces. Results showed that the Tactip could sense changes in force over a range of 0-4.413 N, as the arm moved in steps of 0.5 mm, equivalent to a loading resolution of about 0.1 N at the lowest load and 1 N at the highest load. A pneumatically controllable tactip sensor was shown by Bewley et al. to be able to identify 3 mm pins embedded up to 5 mm deep [11]. The sensor could identify the depth of embedded pins in over 90% of trials. These sensors had diameters over 30 mm, preventing them from being inserted into trocars.

Pressure modulated optical tracking (PMOT) sensors [12], [13] have been shown to be able to measure forces, quantify elasticity and locate boundaries in dynamic palpation. They do this through tracking points on the inside of a membrane,

This work was supported by the U.K. Engineering and Physical Sciences Research Council (EPSRC) under Grants: EP/S014039/1 and UKRI/EP/B000259/1, and by the UCL Therapeutic Acceleration Support Fund under Grant No. 184646.

[1] D.G. Raitt, S.-A. Abad, S. Homer-Vanniasinkam, H.A. Wurdemann are with the Department of Mechanical Engineering, UCL, London, WC1E 7JE, UK. (e-mail: {duncan.raitt.19, s.abad-guaman, s.homer-v, h.wurdemann}@ucl.ac.uk).

[2] P. Dasgupta is with the Department of Urology, Guy's and St Thomas' NHS Trust, London, SE1 9RT, UK. (e-mail: {prokar.dasgupta}@kcl.ac.uk).

[3] S.-A. Abad is with the Facultad Agropecuaria y de Recursos Naturales Renovables, Universidad Nacional de Loja, Loja, 110101, Ecuador.

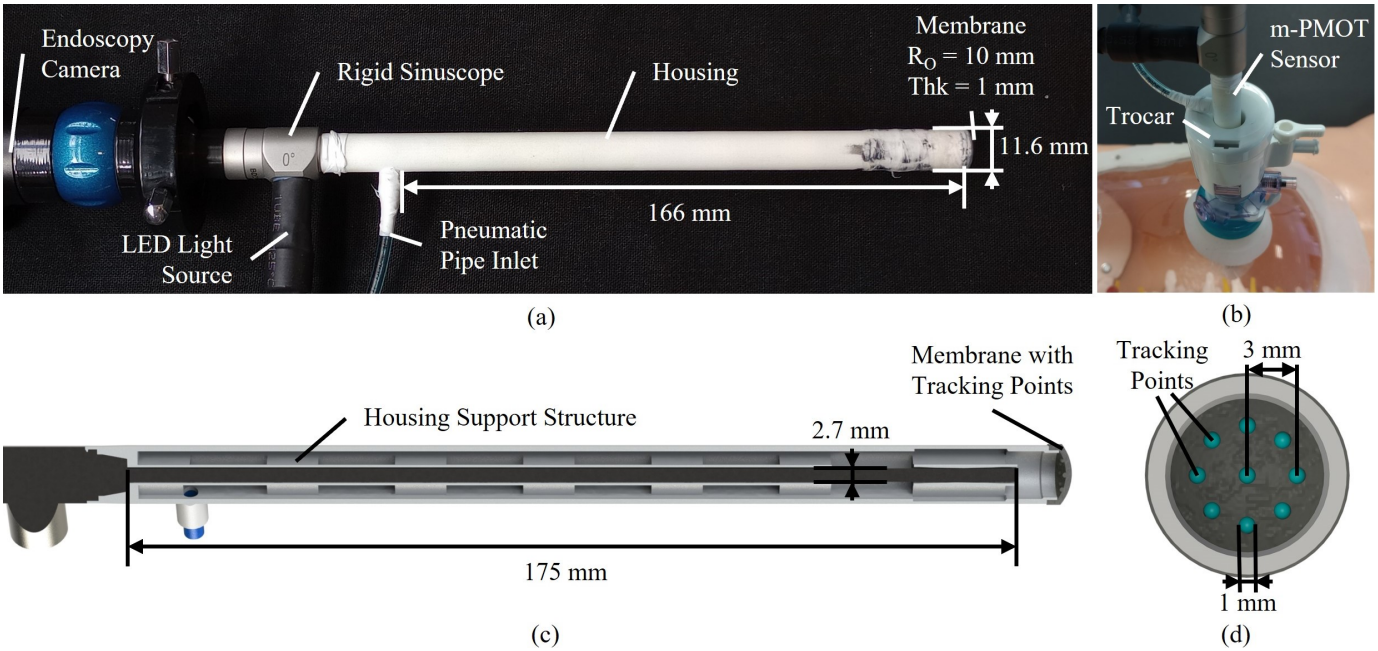

Fig. 1. The m-PMOT with dimensions and parts labelled. Showing photographs of (a) the assembled m-PMOT sensor and (b) the m-PMOT sensor in a trocar, along with CAD-rendered images of (c) a cross-sectional view of the sensor showing the support structure and (d) a view of the inside of the membrane Showing the tracking points.

whilst controlling the compliance of the membrane through internal pressure regulation. In [12], we showed that the PMOT sensor could measure normal forces with a pneumatically controllable force sensing range and measure the angle and magnitude of forces. Across all data, the RMSEs for force, θ_Y and θ_X were 9.86%, 5.26% and 8.35% of their respective ranges. It was further shown in [13] that the PMOT sensor could measure the elasticities of phantoms using a neural network. Phantoms ranging from 4.20 kPa to 177.62 kPa in elasticity were measured with an RMSE of 2.85% of range. This paper also showed that the sensor could locate boundaries between 13.4 kPa elastomer and embedded 29.3 kPa elastomer. This was done both mounted on a linear rail where the SNR was 39.51:1 and an offset of 1.526 mm and in participant-controlled teleoperated palpation where the side on which the boundary was located and the stiffer side of the boundary were located correctly in 96.5% of trials. The PMOT sensors could not be used in MIS applications as they had external diameters of 20 mm. They were also sealed to the camera requiring the entire system to be replaced after use.

Adapting soft multimodal haptic sensors to the minimally invasive surgery (MIS) environment will enable surgeons to locate and identify unhealthy tissue — even when tumours are not visually detectable, such as those beneath the tissue surface — using a single instrument while minimising tissue damage. However, MIS surgical tools are inserted into the patient through trocars [14], [15]. The most common internal diameters for trocars are 5 mm, 10 mm, and 12 mm. None of the devices that demonstrated their ability to measure stiffness or hardness and locate inclusions or boundaries in palpation or pressing have an outer diameter below 12 mm, which prevents them from being used in MIS. Miniaturisation remains a challenge in the development of devices for MIS, especially for those pneumatically actuated [14]. For instance, the miniaturisation of soft actuators developed through the last decade [16]–[18] have been recently achieved [15], [19]. Visual-based sensors are often limited by the size of cameras and the components around them [20]. Meanwhile, other mechatronic systems would require multiple mechanisms to measure these stimuli, increasing their size.

The contribution of this paper lies in the creation of a miniaturised soft tissue stiffness sensor with dimensions that make it suitable for palpation in minimally invasive surgery. The specific novelties of this work are outlined as follows:

1) A stiffness sensor capable of quantifying the mechanical elasticity of soft tissue has been miniaturised to an external diameter of 11.6 mm, making it compatible with standard 12 mm MIS trocars. Notably, this reduction in size is achieved without compromising the sensor's palpation capabilities compared to our previously reported large-scale prototype [12], [13].
2) The stiffness sensor is compatible with standard minimally invasive surgical camera systems, such as a sinuscope, enabling miniaturisation of the sensor through integration with conventional laparoscopic hardware.

The paper is structured as follows: Section II describes the sensing principle and miniaturised soft-tipped sensor design. Section III evaluates its force sensing performance, while Section IV presents stiffness sensing experiments using tissue-mimicking phantoms. Section V reports palpation results, and Section VI analyses the sensor's reach through trocars. Section VII provides a comparative analysis with the large-scale prototype, and Section VIII concludes the paper.

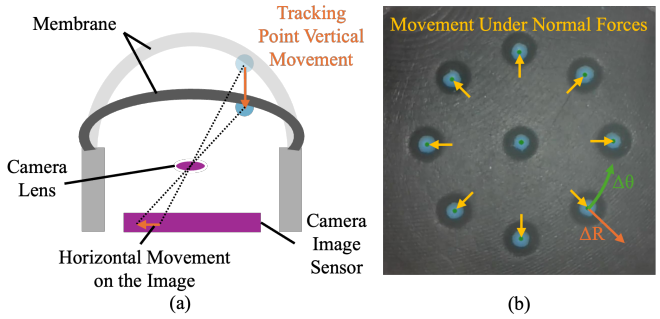

Fig. 2. (a) When the membrane is pressed the tracking points move. Due to the placement of the camera, a vertical movement of a tracking point is seen as a horizontal movement in the image. (b) Tracking points move away from the direction of contact. Hence, under normal forces, they move outwards. The components used for recording tracking point movements, Δr & $\Delta\theta$, are also displayed. Δr records the movement of tracking points away from the central point whilst $\Delta\theta$ records movement around the central point.

II. Sensing Principle and Mechanical Design

A. Sensing Principle

The sensor described in this paper is called the miniaturised pressure modulated optical tracking (m-PMOT) sensor. This sensor functions through the same sensing principle as the sensors in [12] and [13]. Forces acting on the membrane surface cause the tracking points to move away from the force, as shown in Fig. 2. By tracking these points variables like force magnitude, force directions and stiffness can be obtained. The sensor adjusts the compliance of an elastomer membrane through varying the internal pressure. As the internal pressure increases, the membrane compliance decreases due to an increase in internal air mass and an increase in membrane strain. This adjustable compliance allows the sensor to alter its force sensing range. It can also be used to measure tissue stiffness at a single location by varying the compliance and measuring the resulting membrane displacement (see Supplementary Video S1).

B. Sensor Design and Fabrication

The sensor in this paper, shown in Fig. 1, is created by minimising the sensors in [12] and [13] around an ESC Rigid Sinuscope. This sinuscope has an external diameter of 2.7 mm and a length of 175 mm.

A stiff housing with an outer diameter of 11.6 mm was placed over the sinuscope with a membrane attached to its distal end and pneumatic piping inserted into its proximal end. This aligns with the ideal diameter $\geq$ 12 mm for MIS devices [21]. The housing consisted of inner and outer tubes connected by a support structure. This structure stiffened the sensor, ensured the alignment of components even under shear loads, and allowed air to flow from the pneumatic pipe to the membrane. Tolerating of the inner tube was performed to minimise air leakage whilst not damaging the sinuscope. This housing was printed from PA2200 (Nylon 12) on a EOS FORMIGA P 110 printer. The housing was designed so that the sensor could be placed over the sinuscope and clipped into place without any modifications to the sinuscope. This allowed the sensor to be removed for disposal whilst leaving the sinuscope ready for sterilisation.

A soft membrane was cast from a mixture of 10 g of Smooth-On Ecoflex 00-30 to 2 ml of Smooth-On Silc Pig Black. The softer elastomer from [12] was chosen over the elastomer from [13], which had better palpation performance, due to geometric changes stiffening the membrane. The dome-shaped membrane had an outer radius of 10 mm and a thickness of 1 mm. The dome radius had to be decreased to maintain height for force sensing, however, the thickness of the membrane could not be decreased to compensate for the reduction in compliance without hampering manufacturability. It featured nine 1 mm diameter hemispherical tracking points, raised on 0.16 mm cylinders, on its inside, one in the centre and eight in a circle of radius 3 mm. The tracking points had to be scaled down to maintain compliance and accuracy. However, they became less reliably cast and harder to paint when miniaturised which led to the need to raise them on cylinders. These were painted with a mixture of Smooth-On Psycho Paint and Silc Pig Cyan. The manufacturing became less reliable for the miniaturised membrane as a result of the reduction in space for outflow channels from the mould. This led to the need for three elastomer degassing steps in a vacuum chamber, one before pouring, another in the lower mould, and finally after lowering the top mould. The membrane was secured to the housing using instant adhesive and thread seal tape.

Pneumatic piping was inserted and glued into the housing and sealed with silicone sealant. The 4 mm diameter pneumatic pipe was connected to a pressure supply via an SMC ITV0010 pressure regulator which was used to control the internal pressure of the sensor. The sinuscope channelled light to the membrane and transmitted an image of the membrane to an ESC Medicams Portable Endoscopy Camera which fed frames to a computer. To compensate for image distortion from the sinuscope, a camera calibration was carried out using OpenCV. The camera was used to take 25 images of a chessboard. These were run through the *findChessboardCorners* and *calibrateCamera* algorithms to extract the lens distortion coefficients. These were then used to create an undistortion transformation which was applied to every frame before tracking point positions were extracted.

A computer extracted the tracking point positions for each frame sent from the camera. A 7 px by 7 px blur, a cyan extracting colour mask, and a greyscale conversion were applied to the image, before running a Canny edge detection with a threshold of 80 and using the OpenCV *findContours* algorithm to extract borders. Centers of borders with an area of over 90 px were extracted as the positions of the centre of tracking points. The tracking point colour and tracking algorithm were kept as consistent as possible with [12] and [13] to ensure that all changes in performance can be related to design changes.

III. Force Sensing Experiments

An analysis of the m-PMOT sensor's force sensing performance was carried out using the experimental setup

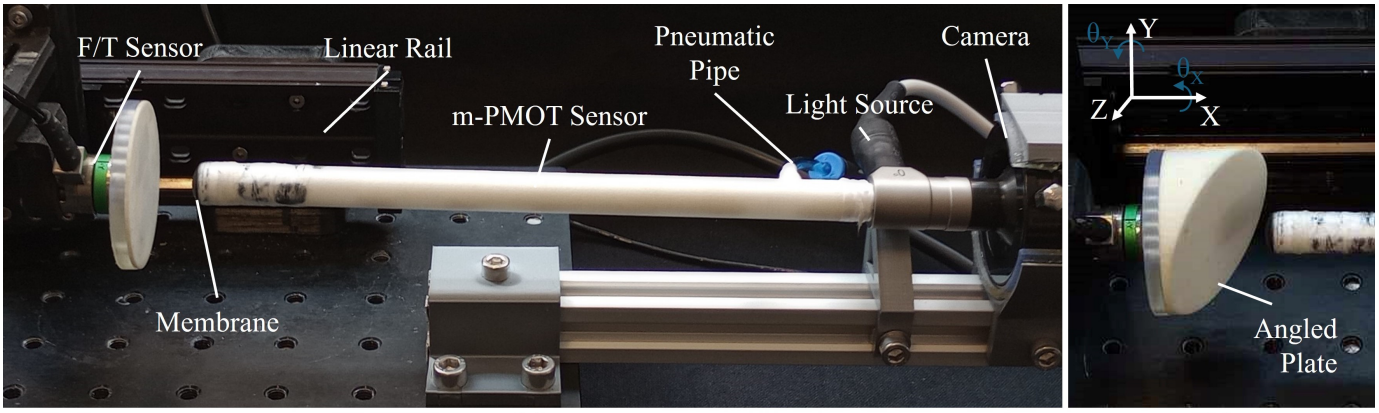

Fig. 3. (a) During force sensing experiments, the m-PMOT sensor membrane was compressed by an F/T sensor mounted on a linear rail. (b) The force angle could be altered by changing or rotating an angled plate in front of the F/T sensor.

presented in Fig. 3 and in line with the experiments run in [13]. This assessed the sensor's ability to adjust its force sensing range in normal force sensing. It further, studied the sensor's accuracy in measuring the angle and magnitude of angled forces. Finally, it also allowed these results to be compared between the m-PMOT sensor and the PMOT sensor in [12].

A. Normal Force Sensing Methodology

The normal force-sensing capabilities of the sensor were assessed by compressing it using a force/torque (F/T) sensor mounted on a linear rail. The internal pressure of the sensor was set with the F/T sensor at a home position 20 mm from the m-PMOT sensor membrane. The F/T sensor moved forward towards the membrane until the contact force reached 0.45 N, it was then moved back 3.5 mm to start the trial out of contact. During the test, the linear rail moved the F/T sensor in 0.05 mm steps towards the m-PMOT sensor. At each step, the movement stopped for 0.1 s to allow the membrane to adjust before collecting four lines of data with 0.01 s of gap between them. Each line of data recorded the F/T sensor outputs in Newtons (N), the position of the linear rail in millimetres (mm) and the m-PMOT sensor tracking point positions in pixels (px). When the force surpassed 2 N the motion was reversed to collect unloading data. This threshold was chosen as, in preliminary testing, it showed clear compression onto the housing lip, surpassing membrane compression. Furthermore, a previous study demonstrated that a sensing range of 0–2 N enables a kinaesthetic palpation probe to detect variations in local tissue stiffness indicative of underlying tumours during lung tumour localization in MIS [22].

The experiment was repeated 15 times at internal pressures of 3.3 kPa, 6.6 kPa, and 9.9 kPa. These pressures were chosen because the membrane-housing seal became less reliable under loads when the internal pressure was above 10 kPa. Ten trials per pressure were used as training data, whilst five were used as testing data. Three priming trials were performed and discarded when the experiment was set up. The displacements of tracking points from their initial positions were converted to polar coordinates around the centre point. The changes in distance from the centre point were averaged to find the mean radial displacement ($\overline{\Delta r}$) measured in pixels (px). To assess the drift of the m-PMOT sensor over time, the experiment was repeated five times at each pressure 8 weeks, 12 weeks and 15 weeks after the initial experiment.

B. Angled Force Sensing Methodology

The experiment in Section III-A was repeated using an angled plate (Fig. 3b) to adjust the force angle. Training, validation and testing data were collected using combinations of X-angles (θ_X), Y-angles (θ_Y), and internal pressures shown in Table I. Ten trials of training, two trials of validation and five trials of testing data were obtained from combinations of internal pressures of 6.6 kPa and 9.9 kPa, X-angles (θ_X) of

TABLE I
ANGLED FORCE SENSING PARAMETER COMBINATIONS

θ_X	θ_Y 0°	5°	10°	15°	20°	25°	30°	Internal Pressure (kPa)
0°	—	‡	—	‡	—	‡	—	6.6
	‡		‡		‡		‡	8.25
	—	‡	—	‡	—	‡	—	9.9
10°			‡		‡		‡	6.6
				•		•		8.25
			‡		‡		‡	9.9
20°			—	‡	—	‡	—	6.6
			‡		‡		‡	8.25
			—	‡	—	‡	—	9.9
30°			‡		‡		‡	6.6
				•		•		8.25
			‡		‡		‡	9.9
40°			—	‡	—	‡	—	6.6
			‡		‡		‡	8.25
			—	‡	—	‡	—	9.9

—	Train and Test Data	‡	Intermediate Test Data	•	Fully Distinct Test Data

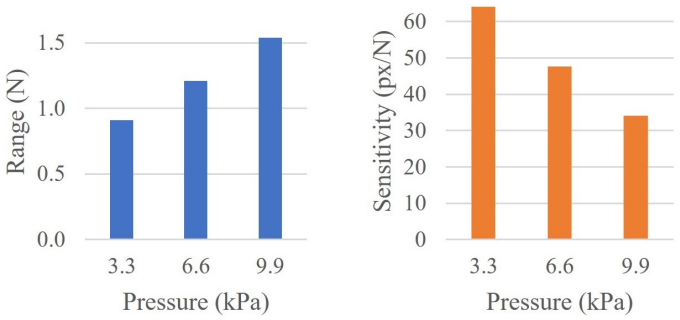

Fig. 4. Normal force sensing range and sensitivity of the m-PMOT sensor with different internal pressures. As internal pressure is increased, the range increases whilst the sensitivity decreases.

0°, 20°, and 40°, and Y-angles (θ_Y) of 0°, 10°, 20°, and 30°. Five trials of testing data were also obtained from intermediate variables: an internal pressure of 8.25 kPa, θ_X of 10°, and 30°, and θ_Y of 5°, 15°, and 25°. At 3.3 kPa the sensor became too flat to measure angles above 15°. Therefore 3.3 kPa was not used for angled force sensing and can only be used for normal or small angle sensing. The θ_X investigated range of up to 40° was chosen to be above the 25° angle of reflectional symmetry of the sensor membrane but below the 50° angle of rotational symmetry. The θ_Y maximum angle of 30° is the upper range of the sensor. The dome construction of the membrane leads to housing contact at low forces when at contract angles above 35°. The studied range covers many MIS scenarios where the surgeon is operating close to normal to the tissue.

The data was cropped between 0.05 N and 1.54 N, the maximum range in Fig. 4. Then, tracking point locations were converted to radial and angular displacements (Δr & $\Delta\theta$) in px and degrees, respectively, from polar coordinate systems around each tracking point. A regression neural network was used to relate tracking point locations to force angles and magnitudes. The inputs were defined as the Δr & $\Delta\theta$ for each tracking point and the pressure (P) in kPa. The outputs were defined as the force (F) in N, and contact angles θ_Y and θ_X in degrees. These were used to train, validate and test a neural network (NN) featuring five hidden fully connected layers, each with 80 nodes using the rectified linear unit (ReLU) activation function. The NN was trained for 50 epochs with validation every 50 iterations. The network with the best validation performance was extracted.

C. Normal Force Sensing Results

Results were processed to investigate how changing the internal pressure of the sensor affects the force sensing range and sensitivity, measure the m-PMOT sensor force sensing parameters, and analyse the sensor accuracy. This was done using only Δr tracking point displacements as $\Delta\theta$ was below 0.0436 Rad in all data.

The range and sensitivity of the sensor were extracted at each internal pressure. The range was defined as the force when the F/T sensor came into contact with the m-PMOT housing. This location was found by carrying out five tests with a depressurised sensor and extracting the position where the force-position gradient exceeded six times the average of

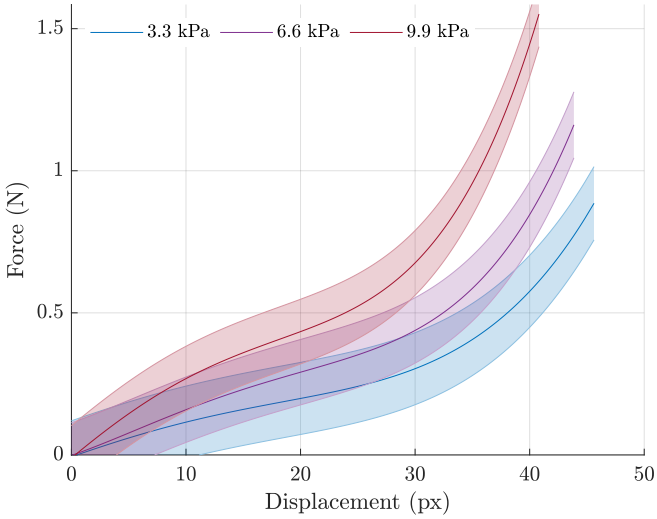

Fig. 5. Force-displacement 4th-order fit at each pressure with confidence intervals. At each pressure, a single value of displacement corresponds to a single value of force. Further, it is demonstrated that the sensitivity at each pressure decreases across its sensing range.

TABLE II
NORMAL FORCE SENSING DATA VARIABILITY WITH INTERNAL PRESSURE

	Internal Pressure		
	3.3 kPa	6.6 kPa	9.9 kPa
∂_4 Adjusted R^2	0.916	0.962	0.978
∂_4 RMSE (N)	0.0646	0.0586	0.0580
∂_4 RMSE (%)	7.10	4.84	3.77

TABLE III
NORMAL FORCE SENSING PARAMETERS

		Internal Pressure		
		3.3 kPa	6.6 kPa	9.9 kPa
Inter-point Deviation	(Mean RMSD %)	3.86	3.79	3.66
	(SD RMSD %)	0.1171	0.0595	0.1264
Non-repeatability	(%)	2.263	2.166	2.199
Hysteresis	(Mean %)	15.81	8.41	5.61
	(SD %)	1.598	0.663	0.378

all preceding gradients. For each pressure, the average force at this position was defined as the range. A best-fit straight line was fitted to $\overline{\Delta r}$-pressure data at each pressure. The sensitivity was extracted as the gradient of this line. The range and sensitivity are displayed at each pressure in Fig. 4.

The sensor $\overline{\Delta r}$-pressure relationship was analysed, and the sensor parameters were extracted. A 4th-order polynomial was fitted to the $\overline{\Delta r}$-pressure training data at each pressure. These fits are shown with 95% confidence intervals in Fig. 5, and the goodness of fit data is shown in Table II. The sensor parameters are shown in Table III. The inter-point deviation was defined as the root-mean-square deviation (RMSD) between $\overline{\Delta r}$ and Δr across all tracking points and data points. Non-repeatability was defined as the maximum deviation between $\overline{\Delta r}$ values at the same position. Hysteresis was calculated by fitting 6th-order polynomials to loading and unloading data for each trial. The largest separation

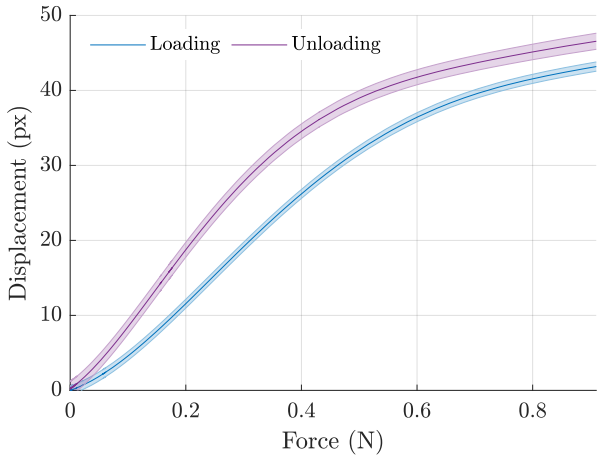

Fig. 6. An example hysteron at an internal pressure of 3.3 kPa. Displacement-Force 6th-order fits with confidence intervals are displayed for loading and unloading data of a single trial over the sensors force sensing range at this pressure.

TABLE IV
NORMAL FORCE SENSING TEST DATA ACCURACY RESULTS COMPARING ALL DATA TO LOADING ONLY DATA

		Internal Pressure		
		3.3 kPa	6.6 kPa	9.9 kPa
Bidirectional Data	RMSE N	0.0853	0.0809	0.0785
	RMSE %	9.31	6.59	5.05
	Max Error %	22.3	18.9	14.4
Loading Data	RMSE N	0.0139	0.0207	0.0160
	RMSE %	3.00	3.07	1.75
	Max Error %	7.32	7.67	6.40

between these fits, extracted at 0.1 N internals, was used to find the mean and SD hysteresis. Hysteresis could not be extracted from raw data because the position control did not lead to identical, repeatable force values. A 6th-order fit was therefore chosen as the polynomial fit with the highest average coefficient of determination (adjusted R^2) when the data was split between loading and unloading. An example of the hysteresis fits at 3.3 kPa is shown in Fig. 6.

The accuracy of the m-PMOT sensor was analysed by comparing the test data to the 4th-order polynomial fits. This model had a higher adjusted R^2 than other polynomial fits. Table IV shows the root-mean-square error (RMSE) and maximum error in Newtons and as a percentage of the range. The same method was used to produce a 4th-order polynomial fit from the training loading data and compare it to testing loading data to analyse the effect of hysteresis.

The drift of the sensor over time was assessed. Table V shows the errors between the data calculated from the base experiment training data 4th-order fit and the testing data for the base experiment, at 8 weeks, 12 weeks and 15 weeks.

D. Angled Force Sensing Results

After the neural network (NN) was trained on training data, its accuracy was assessed using testing data. The RMSE was calculated for groups of trials based on the parameter being varied in comparison to the training data parameters.

TABLE V
NORMAL FORCE SENSING ERRORS WITH TIME

		Internal Pressure		
		3.3 kPa	6.6 kPa	9.9 kPa
RMSE N	Base	0.0853	0.0809	0.0785
	8 Weeks	0.0663	0.0702	0.0857
	12 Weeks	0.0603	0.0579	0.0599
	15 Weeks	0.0641	0.0735	0.1187

Table VI displays the RMSEs in Newtons and degrees, and as a percentage of the tested range. These ranges were 1.54 N, 30° and 40°. The average RMSEs across all data were 0.129 N, 2.01°, and 5.57° for force, θ_Y, and θ_X readings, respectively. These correspond to 8.37%, 6.68%, and 13.92% of their respective ranges.

Confusion matrices were used to present how errors were distributed across angle measurements. These are shown in Table VII and were produced by rounding the angle predicted from the NN to the nearest 5° or 10° and plotting them against the true angle. The effects of the angle and magnitude of forces on errors were analysed. Data was split by force at 0.5 N and by θ_Y between 15° and 20°. This produced four groups; the RMSEs for each group are shown in Table VIII. These relationships were analysed using T-tests. Larger forces produced significantly higher force errors, $t(34110) = 121.48, p < 0.001$, and θ_X errors, $t(34110) = 6.10, p < 0.001$, and lower θ_Y errors, $t(34110) = -9.47, p < 0.001$. Larger θ_Y values correlated significantly with decreased force errors, $t(34110) = -16.06, p < 0.001$, θ_Y errors, $t(34110) = -12.64, p < 0.001$, and θ_X errors, $t(34110) = -9.09, p < 0.001$.

The effects of internal pressure on errors were examined by examining the RMSEs at 6.6 kPa and 9.9 kPa, Table IX. Kolmogorov-Smirnov tests for normality were not passed by any variable at any pressure, therefore, Wilcoxon rank sum tests were carried out between pressures. These showed that the tests at an internal pressure of 9.9 kPa had significantly higher force errors, $z = 8.38, p < 0.001$, and θ_Y errors, $z = 4.92, p < 0.001$, but lower θ_X errors, $z = -8.80, p < 0.001$ than tests at 6.6 kPa.

E. Normal Force Sensing Discussion

Fig. 4 shows that as the internal pressure of the m-PMOT sensor increases, the sensor's force sensing range increases, and its sensitivity decreases. A 4th-order fit can be used to

TABLE VI
ANGLED SENSING NETWORK ACCURACY WITH VARIABLES FROM THE TRAINING SET AND INTERMEDIATE VARIABLES BETWEEN TRAINED VALUES

	Trained	Intermediate			Fully
	Variables	Pressures	θ_Y	θ_X	Intermediate
Force (N)	0.1029	0.1081	0.1898	0.0913	0.1249
RMSE (%)	6.68	7.02	12.32	5.93	8.11
θ_Y (°)	1.16	1.18	3.18	1.21	3.18
RMSE (%)	3.87	3.94	10.61	4.02	10.60
θ_X (°)	3.73	4.06	6.53	7.00	7.61
RMSE (%)	9.33	10.15	16.33	17.49	19.01

TABLE VII
ANGLE SENSING CONFUSION MATRIX
SHOWING THE TRUE VALUE OF THE θ_Y AND θ_X TEST DATA COMPARED TO THE PREDICTED VALUE FROM THE NEURAL NETWORK. ALL VALUES ARE GIVEN AS A PERCENTAGE OF THE TOTAL NUMBER OF DATA POINTS FOR THAT TRUE VALUE.

θ_Y

True Value \ Predicted Value	0	5	10	15	20	25	30
0	99.7	0.3	0.0	0.0	0.0	0.0	0.0
5	1.9	4.6	91.8	0.8	0.9	0.0	0.1
10	0.0	0.1	98.7	0.8	0.4	0.1	0.0
15	0.0	0.0	38.1	49.1	12.4	0.5	0.0
20	0.0	0.2	0.4	3.3	92.5	3.4	0.2
25	0.0	0.0	0.0	0.1	32.7	58.2	8.9
30	0.0	0.0	0.0	0.0	0.1	5.5	94.5

θ_X

True Value \ Predicted Value	0	10	20	30	40
0	90.9	1.8	6.7	0.5	0.1
10	15.9	53.0	30.9	0.2	0.1
20	0.4	0.8	92.5	6.1	0.2
30	0.0	0.2	10.0	25.8	64.0
40	1.1	0.3	0.7	1.2	96.7

relate tracking point displacements to force. As demonstrated in Fig. 5, each displacement measurement correlates to one force value. Table II shows that as the internal pressure of the m-PMOT sensor increased, its force-sensing accuracy did not decrease. This means that whilst the sensitivity can be increased by decreasing the internal pressure, it is negated by the decrease in accuracy. This trend was also seen when fitting training data in Table III, where the variability decreases with pressure. This table shows that whilst there was little change in inter-point deviations and non-repeatability with pressure, the hysteresis decreased as the pressure increased. This table along with the example hysteron in Fig. 6 show that hysteresis has a large effect on the sensor's accuracy. The higher hysteresis

TABLE VIII
RELATIONSHIP BETWEEN ERRORS IN EACH VARIABLE, AND THE MAGNITUDE AND θ_Y OF THE FORCE

	Low θ_Y (0 - 15°)	High θ_Y (20° - 30°)	
No. Data-points	10177	14395	
Force RMSE (N)	0.0728	0.0572	Low Force
θ_Y RMSE (°)	2.46	1.79	(< 0.5 N)
θ_X RMSE (°)	5.92	5.12	
No. Data-points	5231	4309	
Force RMSE (N)	0.204	0.241	High Force
θ_Y RMSE (°)	1.80	1.71	(> 0.5 N)
θ_X RMSE (°)	6.76	4.41	

TABLE IX
ANGLED SENSING ACCURACY WITH PRESSURE

	Internal Pressure	
	6.6 kPa	9.9 kPa
No. Data-points	12156	14164
Force RMSE (N)	0.132	0.134
θ_Y RMSE (°)	2.07	1.96
θ_X RMSE (°)	6.25	5.04

at lower pressures is not present in tests on the PMOT sensor in [12] and is most likely due to the dynamics of the smaller membrane. Table IV shows that when the analysis is restricted to loading data only to remove the effects of hysteresis, the accuracy is best at the lowest pressure. However, the accuracy is worst at 6.6 kPa, showing that there is still not a clear correlation between accuracy and sensitivity. At their max tested pressures, the m-PMOT sensor had a higher RMSE, 5.05% to 4.36% of range, but a lower max error, 14.4% to 21.8% of range, compared to the PMOT sensor. These errors are both lower than RMSE of around 7.5% of range obtained in normal planer force sensing with the gelsight sensor [4].

Table V shows that the m-PMOT sensor's performance fluctuates with time. Results show that over the 15 weeks after the initial base fit, the drift caused the RMSEs to change by less than 0.04 N. The lowest errors at all three pressures were at 12 weeks, whilst the highest errors at 3.3 kPa and 6.6 kPa were in the base experiment and at 9.9 kPa were at 15 weeks. Showing that there was no consistent trend in errors increasing or decreasing over time.

F. Angled Force Sensing Discussion

The m-PMOT sensor's ability to measure the angle and magnitude of forces is demonstrated in Table VI. Trained variables produced the lowest θ_Y and θ_X errors, whilst data with intermediate θ_X values produced the lowest force errors. The low force errors with intermediate θ_X data may be due to this data set also having a higher average θ_Y value. As will be shown later in this discussion, higher θ_Y values correlate with lower force errors. This was in line with intermediate θ_Y data having the highest force measurement errors, and also had a lower average θ_Y value. θ_Y and θ_X measurements had the highest errors with their respective intermediate values and with fully intermediate values. This may be due to the NN pulling these values towards trained values.

Table VII demonstrates that trained angles are identified more accurately than intermediate angles, which are often identified as closer to their nearest trained angle. This suggests that the NN is over-fitting data. θ_Y of 5° data has the lowest accuracy. There was less training and validation data at θ_Y of 0° than at other θ_Y training angles. This may have made the network fit closer to a θ_Y of 10° rather than producing a more linear fit between them. Although this shows that there is room for improvement in the sensor algorithms, many palpation tools only feed the normal force to the surgeon [23]–[25]. Therefore, any level of angle detection could potentially improve the surgeon's ability to locate the edges of tumours.

Table VIII and the related statistical tests prove that at increased force values, the force and θ_X measurement errors are increased whilst the θ_Y errors are decreased. Alongside this, at increased θ_Y values, measurement errors are reduced across all parameters. It should be noted that these correlations are not independent as there is a higher ratio of low-force to high-force data points at high θ_Y values than at low θ_Y values.

The change in sensing accuracy between the two pressures is shown in Table IX. Both the table and the Wilcoxon rank sum tests show an increase in force measurement errors and a decrease in θ_X errors at 9.9 kPa. However, the θ_Y RMSE was lower at 9.9 kPa, whilst the Wilcoxon rank sum test found that the θ_Y errors were higher at 9.9 kPa. RMSE measurements weight extremes and outliers heavily, whilst Wilcoxon rank sum tests compare median values decreasing the weight of extreme values. This suggests that at higher internal pressures, the median θ_Y error increases, whilst an increase in extremely low θ_Y errors decreases the RMSE.

Results were compared to angle force sensing results with the PMOT sensor in [12]. The PMOT sensor RMSEs were 0.276 N, 1.78° and 1.89° respectively, 9.86%, 5.26% and 8.35% of their respective ranges. The m-PMOT sensor RMSEs were 0.129 N, 2.01°, and 5.57°, corresponding to 8.37%, 6.68%, and 13.92% of their respective ranges. This demonstrates that the m-PMOT sensor can measure the magnitude of forces more accurately than the PMOT sensor, but measures the force angle less accurately. This may be due to the m-PMOT sensor having larger tracking points in comparison to the membrane diameter, resulting in them being less sensitive to small changes in angle.

IV. Stiffness Sensing Experiments

An analysis of the m-PMOT sensor's stiffness sensing performance was carried out in line with the experiments run in [13]. This measured the sensor's ability to measure sample elasticity and allowed the stiffness sensing accuracy of the m-PMOT sensor to be compared to the accuracy of the PMOT sensor in [13].

A. Stiffness Sensing Methodology

Phantoms ranging in elasticities between 4.20 kPa and 177.62 kPa were produced from Smooth-on platinum cure elastomers as detailed in [13]. These phantoms were 30 mm in height and had 50 mm in diameter. Samples were split into training phantoms of 4.20 kPa, 9.12 kPa, 13.35 kPa, 29.27 kPa, 63.62 kPa, 111.41 kPa, and 177.62 kPa in elasticity and testing phantoms with elasticities of 7.83 kPa, 12.32 kPa, 22.36 kPa, 42.12 kPa, 85.08 kPa, and 145.72 kPa. These stiffness values cover a large range of tissues shown in Fig. 2 in [13].

The m-PMOT was mounted on a Franka Emika Panda robot and held 10 mm above the phantom. The sensor membrane was parallel to and concentric to the top of the phantom. Optilube medical lubricant was used to cover both the phantom and the membrane. After the tracking point's initial positions were obtained, the sensor was lowered into contact with the phantom. Contact was standardised by measuring the displacements of the eight outer tracking points. The sensor was adjusted to an average displacement of 25-30 pixels.

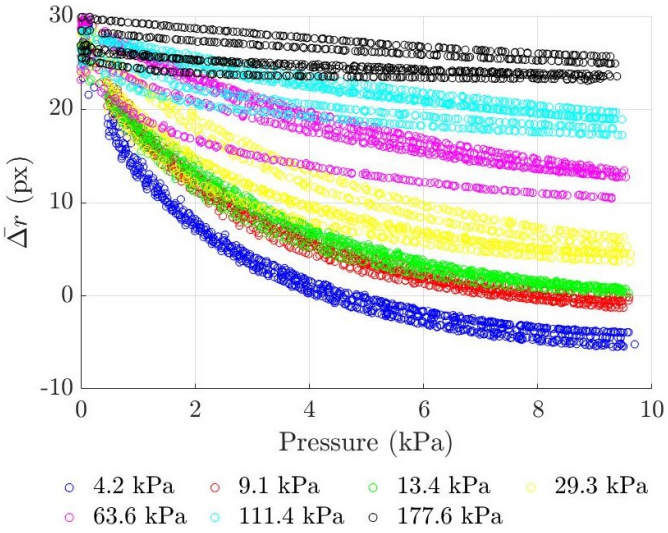

Fig. 7. Raw data during pressurisation in contact with phantoms of different stiffness. Tracking point displacement, $\overline{\Delta r}$, is graphed against the internal pressure of the sensor. Different coloured data-points represent the different stiffnesses of phantoms. The starting gradient of the line changes as the phantom stiffness increases.

To measure the internal pressure-tracking point displacement relationship, the internal pressure was increased to 9.77 kPa in steps of 0.061 kPa. At each step, the pressure was held for 1.5 s whilst the membrane adjusted. Then, the tracking point positions were recorded five times at 0.2 s intervals. The experiment was repeated five times with each training phantom. Tracking point positions were converted to polar coordinates around the central point to find the radial displacements (Δr) in pixels (px). The radial displacements were averaged to produce $\overline{\Delta r}$.

A second experiment was used to quickly quantify stiffness. After contact was made, the pressure was set to 0 kPa, 2 kPa, 4 kPa, and then 6 kPa. At each of these pressures, the membrane was adjusted during a 1 s pause. Then, tracking point locations were sampled 4 times. This produced a mean sampling time of 4.39 s. Lower sets of pressures showed more accurate measurements on low stiffness samples whilst higher pressures were more accurate at measuring high stiffness samples. These pressures were chosen as they showed good accuracy across the training phantoms in preliminary testing. Training phantoms were tested 20 times to produce training data and 4 times for validation data. Both training and testing phantoms were then tested 16 times for testing data. Training data was used to train a feed-forward, fully connected regression neural network (NN). This NN had three hidden layers of five nodes each, all utilising rectified linear unit (ReLU) activation functions. The $\overline{\Delta r}$ at each pressure was input to the network, trained to output elasticity in kPa. A NN was chosen both to be in line with [13], so that any differences observed can be correlated to geometric changes from miniaturisation, and because the NN produced more accurate results than other regression fitting methods including linear, polynomial, and generalized additive model regression.

TABLE X
INITIAL PRESSURE-DISPLACEMENT GRADIENT (UP TO 1 KPA) VS PHANTOM STIFFNESS

	Phantom Stiffness (kPa)						
	4.20	9.12	13.35	29.27	63.62	111.41	177.62
Gradient (px/kPa)	-15.588	-10.220	-8.563	-6.435	-3.566	-2.081	-0.832

B. Stiffness Sensing Results

Fig. 7 shows raw $\overline{\Delta r}$-internal pressure data at each sample elasticity. This demonstrates a unique $\overline{\Delta r}$-pressure curve for each elasticity of phantom. The gradient of a linear fit of this data up to 1 kPa is shown in Table X.

The neural network's (NN) accuracy was assessed by comparing its output to ground truth values. The calculated root-mean-square errors (RMSEs) for each sample are shown in Table XI in Newtons (N) and as a percent (%) of sample stiffness. Across all samples, the RMSE was 11.96 kPa, 6.74% of range, whilst the non-repeatability was 37.4%. The RMSEs of trained and untrained samples were 10.1 kPa and 13.8 kPa, 5.71% and 7.79% of range, respectively. A Pearson product-moment correlation showed that errors increased as phantom stiffness increased, $r(96) = 0.8650, p < 0.001$.

C. Stiffness Sensing Discussion

Fig. 7 and Table X demonstrate that the $\overline{\Delta r}$-pressure relationship can be used to distinguish between phantoms of different stiffness. There is an exponential increase in elasticity between samples. However, the increase in initial gradient between samples was not exponential. This suggests that the change in the change in the $\overline{\Delta r}$-pressure relationship with elasticity is non-linear. Fig. 7 had higher intra-pressure deviations, and lower inter-pressure deviations than were seen in [13]. This suggests that the m-PMOT sensor will measure phantom elasticity less accurately than the PMOT sensor.

The m-PMOT sensor measured the stiffness of phantoms between 4.20 kPa and 177.79 kPa with an average RMSE of 11.96 kPa, 6.73% of the tested range. Testing phantoms were sensed less accurately than training phantoms. Consistent with the trends observed for the large-scale PMOT sensor in [13], absolute errors increased with phantom stiffness.

For one of the untrained phantoms, the RMSE was more than the difference to its preceding trained phantom. Also, the RMSE of three other untrained phantoms was higher than half the difference from their preceding trained phantoms. This suggests that the stiffness sensing accuracy of the m-PMOT sensor cannot reliably differentiate between this phantom set.

The stiffness sensing accuracy was worse with the m-PMOT sensor, RMSE of untrained phantoms = 7.79% of range, than with the PMOT sensor, RMSE of untrained phantoms = 2.85% of range. This is likely due to differences in the structural properties of the membranes of the sensors, especially their compliance. Compared to other sensors in the literature, these errors are higher than the hardness sensing RMSE of the gelsight sensor, 5.95% of range, and higher than the maximum spring stiffness measurement error from Faragasso et al., 6.4% of sample spring stiffness [1], [2]. For one of the untrained phantoms, the RMSE was higher than the difference to its preceding trained phantoms. Additionally, the RMSE of three other untrained phantoms was higher than half the difference to their preceding trained phantoms. This suggests that the stiffness sensing accuracy of the m-PMOT sensor cannot reliably differentiate between this set of phantoms and that the accuracy of the sensor will need to be improved before it can be used to differentiate between tissues in a clinical setting. The accuracy of the sensor for trained phantoms suggests that this could be achieved by algorithm improvements.

TABLE XI
STIFFNESS SENSING ACCURACY

	Trained Phantom Stiffness (kPa)						
	4.20	9.12	13.35	29.27	63.62	111.41	177.62
RMSE (kPa)	0.179	1.157	1.813	0.140	0.352	1.748	26.433
RMSE (%)	4.271	12.685	13.583	0.479	0.553	1.569	14.882

	Untrained Phantoms Stiffness (kPa)					
	7.83	12.32	22.36	42.12	85.08	145.72
RMSE (kPa)	1.361	1.066	6.711	11.716	22.574	21.424
RMSE (%)	17.383	8.649	30.015	27.815	26.532	14.702

V. PALPATION EXPERIMENT

An experiment was carried out to assess the m-PMOT's ability to locate embedded boundaries during palpation. This experiment was carried out in line with the linear rail palpation experiment in [13].

A. Palpation Methodology

The m-PMOT sensor's accuracy for locating boundaries during palpation was experimentally evaluated. Palpation was assessed on a linear rail but not with participants because extensive training would be required to prevent participants from damaging the sinuscope. Smooth-On elastomers of 13.4 kPa, 22.4 kPa and 29.3 kPa were used to produce stadium-shaped phantoms. The phantoms were half-filled with a softer elastomer and half-filled with a stiffer elastomer embedded 2 mm, 4 mm, or 6 mm under the softer elastomer.

Fig. 8 shows the setup for the experiment. The m-PMOT sensor was mounted on a linear rail above the phantom. Both were covered in a thin layer of medical lubricant to reduce shear forces. The internal pressure (P) of the sensor was set. Then, the sensor was lowered to the preloaded force (F_0). The sensor was moved from 25 mm left of the boundary (Fig. 8 A) to 25 mm right of the boundary (Fig. 8 B) and back (Fig. 8 B-A). At the end of each movement, 5.9 mm shear reversal movements (denoted as SRM in Fig. 8) were used to reverse the shear on the membrane. The linear rail position, tracking point locations and internal pressure were sampled at a $5\,\mathrm{Hz}$ frequency. Every five readings were averaged to reduce the effect of outliers.

The experiment was repeated with different parameter configurations shown next to the corresponding results in Table XII. These configurations are made by varying the parameters:
E_1 - Elasticity of the softer material.
E_2 - Elasticity of the stiffer material.

TABLE XII
MARGIN SENSING TRIALS

	Input Parameters							Outputs		
Conf. #	E_1 (kPa)	E_2 (kPa)	D (mm)	P (kPa)	F_0 (mN)	Speed (mm/s)	Sensor Orientation	Soft-Stiff SNR F	Stiff-Soft SNR F	Mean Offset (mm)
1	13.4	29.3	2	5	50	0.75	Forward	46.79:1	67.28:1	0.660
2	13.4	29.3	2	6	50	0.75	Forward	59.19:1	94.90:1	0.709
3	13.4	29.3	2	7	50	0.75	Forward	37.83:1	52.31:1	0.677
4	13.4	29.3	2	6	40	0.75	Forward	50.77:1	70.18:1	0.970
5	13.4	29.3	2	6	60	0.75	Forward	64.40:1	89.16:1	1.165
6	13.4	29.3	2	6	50	0.50	Forward	66.01:1	86.47:1	0.623
7	13.4	29.3	2	6	50	1.00	Forward	45.27:1	73.28:1	1.046
8	13.4	29.3	2	6	50	0.75	Backward	62.23:1	78.00:1	0.713
9	13.4	22.4	2	6	50	0.75	Forward	18.92:1	43.22:1	0.359
10	13.4	22.4	2	5	50	0.75	Forward	15.34:1	32.64:1	0.478
11	13.4	22.4	2	7	50	0.75	Forward	16.43:1	40.08:1	0.462
12	13.4	22.4	2	6	40	0.75	Forward	17.63:1	35.43:1	0.465
13	13.4	22.4	2	6	60	0.75	Forward	20.20:1	36.23:1	0.316
14	22.4	29.3	2	6	50	0.75	Forward	10.02:1	16.04:1	0.413
15	22.4	29.3	2	5	50	0.75	Forward	10.15:1	17.11:1	0.387
16	22.4	29.3	2	7	50	0.75	Forward	8.46:1	12.22:1	0.776
17	22.4	29.3	2	6	40	0.75	Forward	8.64:1	14.28:1	0.514
18	22.4	29.3	2	6	60	0.75	Forward	10.66:1	16.22:1	0.519
19	13.4	29.3	4	6	50	0.75	Forward	26.33:1	29.60:1	0.550
20	13.4	29.3	4	5	50	0.75	Forward	27.35:1	31.01:1	0.565
21	13.4	29.3	4	7	50	0.75	Forward	22.48:1	30.30:1	0.623
22	13.4	29.3	4	6	40	0.75	Forward	22.61:1	28.08:1	0.556
23	13.4	29.3	4	6	60	0.75	Forward	32.56:1	38.14:1	0.727
24	13.4	29.3	6	6	50	0.75	Forward	17.51:1	25.67:1	0.710
25	13.4	29.3	6	5	50	0.75	Forward	16.36:1	25.51:1	0.887
26	13.4	29.3	6	7	50	0.75	Forward	17.34:1	26.15:1	0.680
27	13.4	29.3	6	6	40	0.75	Forward	14.71:1	20.95:1	0.670
28	13.4	29.3	6	6	60	0.75	Forward	20.26:1	25.57:1	0.829

- Configuration 2, highlighted in grey, contains the baseline parameters.
- The varied parameter in each test is highlighted in orange.
- Soft-Stiff results are obtained by passing the sensor from the softer to the stiffer material (Fig. 8. A to B).
- Stiff-Soft results are obtained by passing the sensor from the stiffer to the softer material (Fig. 8. B to A).
- Offset is the distance between the margin and the middle of the signal.

D - Depth that the stiff material is embedded below the soft material.
P - Pressure inside the m-PMOT sensor.
F_0 - Preloaded sensor force in the sample.
$Speed$ - Linear rail velocity moving the sensor.
$Sensor\,Orientation$ - Orientation at which the sensor was mounted.

With regards to the orientation, the sensor is either mounted forward, with the top of the camera towards the rail, or backwards, with the top of the camera away from the rail. Reversing the sensor orientation switched the leading and trailing edges of the sensor.

The experiment was repeated three times in each configuration. The first movement in each direction was discarded, leaving 12 passes per direction per configuration. Baseline parameters, highlighted in grey in Table XII, were found from preliminary testing.

Preliminary testing repeated the experiment using the E_1 = 13.4 kPa, E_2 = 29.3 kPa, D = 2 mm sample. The parameters were altered, P ranging from 4 kPa to 8 kPa in steps of 1 kPa, F ranging from 30 mN to 90 mN in steps of 5 mN, and Speed ranging from 0.25 mm/s to 1 mm/s in steps of 0.25 mm/s. The parameter combination with the highest signal-to-noise ratio (SNR) was used as the baseline parameter. The tracking point locations were converted to $\overline{\Delta r}$ using the method in Section III-A. This was converted to a force in N using a 4th-order polynomial relationship trained through the method described in Section III-C.

B. Palpation Results

The data was split into the signal section within 10 mm of the boundary and the noise sections on either side of this. The signal was extracted as the amplitude of the data in the signal section, whilst the noise was calculated as the root mean square deviation (RMSD) of the noise segments. The signal was divided by the noise to find the signal-noise ratio (SNR). The middle of the signal was found by fitting eight points on each side of half the signal amplitude with a linear fit. The half of the distance between where the fits for each pass direction intercepted half the signal amplitude was extracted as the offset in mm. The SNR in each direction and mean offset for each parameter combination are shown in Table XII.

C. Palpation Discussion

Table XII's results show that across all configurations, the signal is more than eight times larger than the noise. The baseline parameters (Conf. 2) produced an average SNR

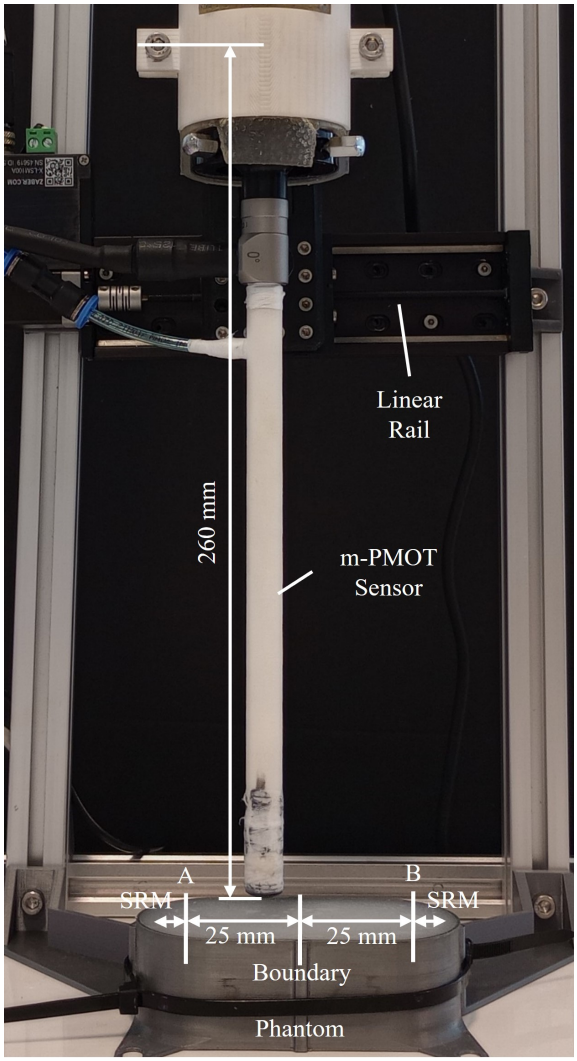

Fig. 8. Experimental setup for boundary location during dynamic palpation. The m-PMOT sensor is mounted on a linear rail above a stadium-shaped phantom. The sensor was lowered and moved across the phantom, from A to B, and back, from B to A. Shear reversal movements (SRM) were performed at each end of the movement.

of 77.04:1 and a mean offset of 0.706 mm. When P, F_0 and speed were increased and decreased from the baseline parameters (Conf. 1 & 3-7), the average SNR decreased. This demonstrates that the baseline parameters were a local optimum of the investigated parameters.

When the difference between the elastomers was decreased by decreasing E_2 (Conf. 9) or increasing E_1 (Conf. 14), the SNR decreased. When E_2 was decreased (Conf. 9-13), no parameter set had a higher SNR than the baseline parameters (Conf. 9). However, when the elasticity of E_1 was increased (Conf. 14-18), decreasing the pressure (Conf. 15) or increasing the force (Conf. 18) increased the mean SNR. Further analysis of the data showed that in both configurations (Conf. 15 & 18), the noise and signal are both increased, with the signal being increased more than the noise.

When the embedded depth was increased, the SNR was increased at decreased pressures at a depth of 4 mm but at increased pressures at a depth of 6 mm. At both increased depths, raising the initial force increased the SNR whilst also increasing the offset.

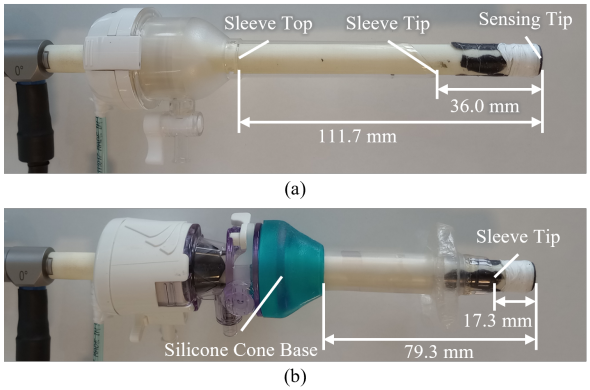

Fig. 9. Sensor in Trocar Cannulas. Measurements of the m-PMOT sensor inside the (a) Vaxcon Safepass Trocar and (b) Applied Medical Kii Balloon Blunt-Tip Access System.

VI. Analysis of the Sensor's Reach Through Trocars

An analysis was performed to evaluate the sensor's reach when operated through trocar access ports. The study combined direct measurements and mathematical analysis of the m-PMOT sensor in trocars.

The sensor was tested with two cannulas: the Vaxcon Safepass Trocar (75 mm sleeve length) and the Applied Medical Kii Balloon Blunt-Tip Access System (100 mm sleeve length). The latter includes a gel cone and suture ties, which were expected to constrain the sensor's range, see Fig. 9.

For each trocar, the distance between the sensing tip and the sleeve tip was measured, along with the maximum insertion reach from the upper reference point of the access port to the sensor tip. The upper reference was defined as the top of the sleeve for the Vaxcon model and the uppermost position of the silicone cone for the Applied Medical model.

At its maximum reach or insertion limit, the sensor would have no stroke along a normal surface. Then, assuming the insertion movement of the trocar remains fixed and only the sensor translates vertically from its uppermost position to the sleeve tip, the maximum flat working diameter D_w can be derived using Equation 1.

$$D_w = 2 * \sqrt{r^2 - (r - h)^2} \tag{1}$$

r denotes the reach of the sensor from the insertion point, and h represents the height between the sleeve tip and the sensing tip. Substituting the measured values into the equation yields a D_w maximum of 164 mm for the Vaxcon trocar and 98.9 mm for the Applied Medical trocar. At the periphery of these flat areas, the corresponding contact angles between the sensor and a flat surface are 47.3° and 38.6°, respectively. When constrained to the 30° contact angle (θ_X) conditions described in Section III, the diameters reduce to 111.7 mm and 79.3 mm, respectively.

The palpation areas of 9799 mm^2 and 4939 mm^2 will cover a large proportion of the areas of spleens, kidneys and livers,

TABLE XIII
COMPARISON BETWEEN LARGE AND MINIMISED PMOT SENSORS

	PMOT Sensor	m-PMOT Sensor
Design		
Diameter (mm)	20	11.6
Removable	No	Yes
Angled Force Sensing		
Force RMSE (%)	9.86	8.37
θ_Y RMSE (%)	5.26	6.68
θ_X RMSE (%)	8.35	13.92
Elasticity Test Data Measurement		
RMSE (%)	2.85	7.79
13.4 kPa to 2 mm embedded 29.3 kPa Palpation		
SNR	38.15:1	77.04:1
Offset (mm)	1.526	0.706

which have areas of around 4884 mm^2, 3189 mm^2 and 16550 mm^2 respectively [26], [27]. A longer and/or articulated sensor would enable palpation across larger surface areas, facilitating the detection of wider or more laterally distributed tumours. Increasing the length of the sensor will not affect the focal length or field of view of the embedded camera, and therefore will not compromise accuracy. The optical systems used in laparoscopes and sinuscopes are designed so that focal length and field of view can be adjusted independently of scope length. The focal length is controlled by the objective lens, while relay lenses take the light up to the scope. There will be device-to-device variation depending on the specific objective lenses used, but this variation is not correlated with length.

VII. COMPARISON BETWEEN PMOT SENSORS

Table XIII summarises the performance differences between the PMOT and m-PMOT sensors. The m-PMOT sensor is smaller with an outer diameter of 11.6 mm, allowing it to fit in a trocar port for MIS and it is removable from the camera, allowing for disposal of the sensor whilst retaining the camera. The m-PMOT sensor elasticity measurement accuracy was lower than that of the PMOT sensor. The m-PMOT sensor showed comparable angled force sensing results and better palpation results than the PMOT sensor. The SNR was higher, 77.04:1 to 38.15:1, and the offset was lower, 0.706 mm to 1.526 mm, when using the m-PMOT sensor compared to the PMOT sensor. This demonstrated that the m-PMOT sensor can locate boundaries both more clearly and more accurately than the PMOT sensor.

VIII. CONCLUSION AND FUTURE WORK

This paper presents the design, fabrication, and evaluation of a miniaturized stiffness sensor capable of passing through trocars with diameters of 12 mm or greater, making it suitable for palpation in minimally invasive surgery. The sensor operates by measuring deformations of a compliance-controllable membrane.

The m-PMOT sensor hardware incorporates an off-the-shelf sinuscope and features a removable housing with an external diameter of 11.6 mm. This design facilitates integration with conventional camera systems. The removable housing allows the camera to be retained while the housing is discarded, enabling camera sterilization and reuse with a new housing for different patients.

Performance evaluations of the m-PMOT sensor demonstrated comparable angled force sensing and superior palpation capabilities compared to the original PMOT sensor. However, its elasticity measurement accuracy was lower, indicating a key area for improvement in future work.

Future work should focus on enhancing sensor performance and evaluating the sensor in environments that more accurately simulate MIS. Many of the models used in this study exhibited overfitting. Therefore, further research should aim to improve these models to achieve more consistent performance. In addition, future studies should investigate the impact of design factors, such as alternative tracking methods and membrane geometries, on sensor performance.

Surgeons are interested in understanding contact at all angles at the surgical site. Additionally, MIS limits the approach angles of tools, increasing the requirement for sensing at high contact angles [28]. The sensor design should be altered to allow force measurements up to 75° from the normal plane to allow for high manipulation angles [29]. Further, in MIS, the surgeons' movement is restricted by the trocar to rotations around a point. This should be reflected in the experimental setup. This could be paired with modifying the sensor to function with an articulating laparoscopic camera to maintain normal contact. In addition, it is important to investigate how fingertip interfaces that provide haptic feedback [30] influence surgical performance when integrated with data collected by the m-PMOT sensor.

REFERENCES

[1] A. Faragasso, J. Bimbo, A. Stilli, H. A. Wurdemann, K. Althoefer, and H. Asama, "Real-time vision-based stiffness mapping," *Sensors (Basel)*, vol. 18, no. 5, 2018. [Online]. Available: https://www.ncbi.nlm.nih.gov/pubmed/29701704

[2] W. Yuan, C. Zhu, A. Owens, M. A. Srinivasan, and E. H. Adelson, "Shape-independent hardness estimation using deep learning and a gelsight tactile sensor," *IEEE International Conference on Robotics and Automation*, pp. 951–958, 2017.

[3] X. Jia, R. Li, M. A. Srinivasan, and E. H. Adelson, "Lump detection with a gelsight sensor," pp. 175–179, 2013.

[4] W. Yuan, S. Dong, and E. H. Adelson, "Gelsight: High-resolution robot tactile sensors for estimating geometry and force," *Sensors (Basel)*, vol. 17, no. 12, 2017. [Online]. Available: https://www.ncbi.nlm.nih.gov/pubmed/29186053

[5] N. Herzig, P. Maiolino, F. Iida, and T. Nanayakkara, "A variable stiffness robotic probe for soft tissue palpation," *IEEE Robotics and Automation Letters*, vol. 3, no. 2, pp. 1168–1175, 2018.

[6] N. Herzig, L. He, P. Maiolino, S.-A. Abad, and T. Nanayakkara, "Conditioned haptic perception for 3d localization of nodules in soft tissue palpation with a variable stiffness probe," *PloS one*, vol. 15, no. 8, p. e0237379, 2020.

[7] W. Li, M. Wang, J. Li, Y. Su, D. K. Jha, X. Qian, K. Althoefer, and H. Liu, "L^3 f-touch: A wireless gelsight with decoupled tactile and three-axis force sensing," *IEEE Robotics and Automation Letters*, vol. 8, no. 8, pp. 5148–5155, 2023.

[8] L. Zhenyu, L. Zihan, Z. Xingyu, L. Yan, D. Yuming, and Y. Tianyu, "3d force identification and prediction using deep learning based on a gelsight-structured sensor," *Sensors and Actuators A: Physical*, vol. 367, p. 115036, 2024. [Online]. Available: https://www.sciencedirect.com/science/article/pii/S0924424724000293

[9] O. C. Kara, N. Venkatayogi, N. Ikoma, and F. Alambeigi, "A reliable and sensitive framework for simultaneous type and stage detection of colorectal cancer polyps." *Annals of biomedical engineering*, vol. 51, no. 7, pp. 1499–1512, 2023.

[10] M. E. Giannaccini, S. Whyle, and N. F. Lepora, "Force sensing with a biomimetic fingertip," in *Conference on Biomimetic and Biohybrid Systems*, vol. 9793, 2016, pp. 436–440.
[11] J. Bewley, G. P. Jenkinson, and A. Tzemanaki, "Optical-tactile sensor for lump detection using pneumatic control," *Frontiers in Robotics and AI*, vol. 8, p. 199, 2021. [Online]. Available: https://www.frontiersin.org/article/10.3389/frobt.2021.672315
[12] D. G. Raitt, S.-A. Abad, S. Homer-Vanniasinkam, and H. A. Wurdemann, "Soft, stiffness-controllable sensing tip for on-demand force range adjustment with angled force direction identification," *IEEE Sens. Journal*, vol. 22, no. 9, pp. 8418–8427, 2022.
[13] D. G. Raitt, M. Huseynov, S. Homer-Vanniasinkam, H. A. Wurdemann, and S.-A. Abad, "Soft-tipped sensor with compliance control for elasticity sensing and palpation," *IEEE Transactions on Robotics*, vol. 40, pp. 2430–2441, 2024.
[14] S.-A. Abad, A. Arezzo, S. Homer-Vanniasinkam, and H. A. Wurdemann, "Chapter 4 - soft robotic systems for endoscopic interventions," in *Endorobotics*, L. Manfredi, Ed. Academic Press, 2022, pp. 61–93.
[15] J. Shi, S.-A. Abad, A. Menciassi, K. Althoefer, and H. A. Wurdemann, "Miniaturised soft manipulators with reinforced actuation chambers on the sub-centimetre scale," in *2024 IEEE 7th International Conference on Soft Robotics (RoboSoft)*, 2024, pp. 157–164.
[16] A. Stilli, H. A. Wurdemann, and K. Althoefer, "Shrinkable, stiffness-controllable soft manipulator based on a bio-inspired antagonistic actuation principle," in *2014 IEEE/RSJ International Conference on Intelligent Robots and Systems*, 2014, pp. 2476–2481.
[17] J. Shi, S.-A. Abad, J. S. Dai, and H. A. Wurdemann, "Position and orientation control for hyperelastic multisegment continuum robots," *IEEE/ASME Transactions on Mechatronics*, vol. 29, no. 2, pp. 995–1006, 2024.
[18] J. Shi, A. Shariati, S.-A. Abad, Y. Liu, J. S. Dai, and H. A. Wurdemann, "Stiffness modelling and analysis of soft fluidic-driven robots using lie theory," *The International Journal of Robotics Research*, vol. 43, no. 3, pp. 354–384, 2024.
[19] J. Shi, S.-A. Abad, G. Shi, W. Gaozhang, J. S. Dai, and H. A. Wurdemann, "Model-based static compliance analysis and control for pneumatic-driven soft robots," *IEEE/ASME Transactions on Mechatronics*, pp. 1–12, 2025.
[20] A. Faragasso, J. Bimbo, A. Yamashita, and H. Asama, "Disposable stiffness sensor for endoscopic examination," *Annual International Conference of the IEEE Engineering in Medicine and Biology Society.*, 2018.
[21] A. L. Trejos, A. Escoto, M. D. Naish, and R. V. Patel, "Design and evaluation of a sterilizable force sensing instrument for minimally invasive surgery," *IEEE Sensors Journal*, vol. 17, no. 13, pp. 3983–3993, 2017.
[22] G. L. McCreery, A. L. Trejos, M. D. Naish, R. V. Patel, and R. A. Malthaner, "Feasibility of locating tumours in lung via kinaesthetic feedback," *The International Journal of Medical Robotics and Computer Assisted Surgery*, vol. 4, no. 1, pp. 58–68, 2008.
[23] P. Puangmali, H. Liu, K. Althoefer, and L. D. Seneviratne, "Optical fiber sensor for soft tissue investigation during minimally invasive surgery," in *2008 IEEE International Conference on Robotics and Automation*, May 2008, pp. 2934–2939.
[24] D. Zbyszewski, P. Polygerinos, L. D. Seneviratne, and K. Althoefer, "A novel mri compatible air-cushion tactile sensor for minimally invasive surgery," in *2009 IEEE/RSJ International Conference on Intelligent Robots and Systems*, Oct 2009, pp. 2647–2652.
[25] S. McKinley, A. Garg, S. Sen, R. Kapadia, A. Murali, K. Nichols, S. Lim, S. Patil, P. Abbeel, A. M. Okamura, and K. Goldberg, "A single-use haptic palpation probe for locating subcutaneous blood vessels in robot-assisted minimally invasive surgery," *2015 IEEE International Conference on Automation Science and Engineering*, 2015.
[26] B. Johnson, S. Campbell, and N. Campbell-Kyureghyan, "Characterizing the material properties of the kidney and liver in unconfined compression and probing protocols with special reference to varying strain rate," *Biomechanics*, vol. 1, no. 2, pp. 264–280, 2021. [Online]. Available: https://www.mdpi.com/2673-7078/1/2/22
[27] O. Ehimwenma and M. Tagbo, "Determination of normal dimension of the spleen by ultrasound in an endemic tropical environment," *Nigerian Medical Journal*, vol. 52, no. 3, p. 198–203, Nov. 2011. [Online]. Available: https://www.ajol.info/index.php/nmj/article/view/71548
[28] T. Li, A. Pan, and H. Ren, "Reaction force mapping by 3-axis tactile sensing with arbitrary angles for tissue hard-inclusion localization," *IEEE Transactions on Biomedical Engineering*, vol. 68, no. 1, pp. 26–35, 2021.
[29] A. N. Supe, G. V. Kulkarni, and P. A. Supe, "Ergonomics in laparoscopic surgery," *J. Minim. Access Surg.*, vol. 6, no. 2, pp. 31–36, Apr. 2010.
[30] S.-A. Abad, N. Herzig, D. Raitt, M. Koltzenburg, and H. Wurdemann, "Bioinspired adaptable multiplanar mechano-vibrotactile haptic system," *Nature Communications*, vol. 15, no. 1, p. 7631, 2024.